Ca^{2+}-binding protein 2 inhibits Ca^{2+}-channel inactivation in mouse inner hair cells

Maria Magdalena Picher[a,b,c,d,1], Anna Gehrt[a,e], Sandra Meese[a], Aleksandra Ivanovic[f], Friederike Predoehl[a], SangYong Jung[a,d,g,h], Isabelle Schrauwen[i,j], Alberto Giulio Dragonetti[k], Roberto Colombo[l,m], Guy Van Camp[i], Nicola Strenzke[e], and Tobias Moser[a,b,c,d,f,g,1]

[a]Institute for Auditory Neuroscience and InnerEarLab, University Medical Center Goettingen, 37099 Goettingen, Germany; [b]Goettingen Graduate School for Neurosciences, Biophysics, and Molecular Biosciences, University of Goettingen, 37077 Goettingen, Germany; [c]Bernstein Center for Computational Neuroscience, University of Goettingen, 37077 Goettingen, Germany; [d]Synaptic Nanophysiology Group, Max Planck Institute for Biophysical Chemistry, 37077 Goettingen, Germany; [e]Auditory Systems Physiology Group, InnerEarLab, Department of Otolaryngology, University of Goettingen Medical Center, 37075 Goettingen, Germany; [f]Max Planck Institute for Experimental Medicine, 37075 Goettingen, Germany; [g]Center for Nanoscale Microscopy and Molecular Physiology of the Brain, University of Goettingen, 37075 Goettingen, Germany; [h]Neuro Modulation and Neuro Circuitry Group, Biomedical Sciences Institutes, Singapore Bioimaging Consortium, Biomedical Sciences Institutes, 138667 Singapore; [i]Department of Medical Genetics, University of Antwerp, 2610 Antwerp, Belgium; [j]Neurogenomics Division, Translational Genomics Research Institute, Phoenix, AZ 85004; [k]Otorhinolaryngology, Department of Surgery, Niguarda Ca' Granda Metropolitan Hospital, 20162 Milan, Italy; [l]Center for the Study of Rare Hereditary Diseases, Niguarda Ca' Granda Metropolitan Hospital, 20162 Milan, Italy; and [m]Institute of Clinical Biochemistry, Catholic University of the Sacred Heart, 00198 Rome, Italy

Edited by A. J. Hudspeth, The Rockefeller University, New York, NY, and approved January 5, 2017 (received for review October 21, 2016)

Ca^{2+}-binding protein 2 (CaBP2) inhibits the inactivation of heterologously expressed voltage-gated Ca^{2+} channels of type 1.3 ($Ca_V1.3$) and is defective in human autosomal-recessive deafness 93 (DFNB93). Here, we report a newly identified mutation in *CABP2* that causes a moderate hearing impairment likely via nonsense-mediated decay of CABP2-mRNA. To study the mechanism of hearing impairment resulting from *CABP2* loss of function, we disrupted *Cabp2* in mice ($Cabp2^{LacZ/LacZ}$). CaBP2 was expressed by cochlear hair cells, preferentially in inner hair cells (IHCs), and was lacking from the postsynaptic spiral ganglion neurons (SGNs). $Cabp2^{LacZ/LacZ}$ mice displayed intact cochlear amplification but impaired auditory brainstem responses. Patch-clamp recordings from $Cabp2^{LacZ/LacZ}$ IHCs revealed enhanced Ca^{2+}-channel inactivation. The voltage dependence of activation and the number of Ca^{2+} channels appeared normal in $Cabp2^{LacZ/LacZ}$ mice, as were ribbon synapse counts. Recordings from single SGNs showed reduced spontaneous and sound-evoked firing rates. We propose that CaBP2 inhibits $Ca_V1.3$ Ca^{2+}-channel inactivation, and thus sustains the availability of $Ca_V1.3$ Ca^{2+} channels for synaptic sound encoding. Therefore, we conclude that human deafness DFNB93 is an auditory synaptopathy.

Ca^{2+} channel | inner hair cell | ribbon synapse | synaptopathy | hearing impairment

Hearing relies on faithful transmission of information at ribbon synapses between inner hair cells (IHCs) and spiral ganglion neurons (SGNs; recently reviewed in refs. 1, 2). Ca^{2+} channels at the IHC presynaptic active zone are key signaling elements because they couple the sound-evoked IHC receptor potential to the release of glutamate. IHC Ca^{2+}-channel complexes are known to contain $Ca_V1.3$ α1 subunit (Cav1.3α1) (3–5), beta-subunit 2 ($Ca_V\beta2$) (6), and alpha2–delta subunit 2 (α2δ2) (7) to activate at around −60 mV (8–10), and are partially activated already at the IHC resting potential in vivo [thought to be between −55 and −45 mV (11, 12)], thereby mediating "spontaneous" glutamate release during silence (13).

Compared with $Ca_V1.3$ channels studied in heterologous expression systems, $Ca_V1.3$ channels in IHCs show little inactivation, which has been attributed to inhibition of calmodulin-mediated Ca^{2+}-dependent inactivation (CDI) (14–17) by Ca^{2+}-binding proteins (CaBPs) (18, 19) and/or the interaction of the distal and proximal regulatory domains of the $Ca_V1.3\alpha1$ C terminus (20–22). This "noninactivating" phenotype of IHC $Ca_V1.3$ enables reliable excitation-secretion coupling during ongoing stimulation (23–25). In fact, postsynaptic spike rate adaptation during ongoing sound stimulation is thought to reflect primarily presynaptic vesicle pool depletion, with minor contributions of $Ca_V1.3$ inactivation or AMPA-receptor desensitization (23–26). CaBPs are calmodulin-like proteins that use three functional out of four helix–loop–helix domains (EF-hand) for Ca^{2+} binding (27). They are thought to function primarily as signaling proteins (28) and differentially modulate calmodulin effectors (29, 30). In addition, CaBPs might also contribute in buffering free cytosoloic Ca^{2+} ions, as do other small EF-hand calcium-binding proteins, such as calretinin, calbindin–D-28k, and parvalbumin-α (31–33). The relevance of the individual CaBPs expressed in IHCs [CaBP1, CaBP2, CaBP4, and CaBP5 (18, 19, 34)] for inhibiting CDI and for hearing is not understood well. Genetic disruption of *Cabp4* in mice caused a very modest increase in CDI of IHC Ca^{2+} influx and left hearing intact (18).

Recently, a mutation in the *CABP2* gene was shown to cause recessive sensorineural hearing impairment [DFNB93 (35)]. Specifically, this splice site mutation in *CABP2* is thought to cause a frameshift resulting in a premature truncation of a CaBP2 amino acid sequence lacking the C-terminal EF hands 3 and 4. The truncated CaBP2 less potently inhibited $Ca_V1.3$ inactivation when studied in HEK293-T cells. This observation suggested that enhanced inactivation of $Ca_V1.3$ channels might

Significance

Ca^{2+} channels mediate excitation-secretion coupling and show little inactivation at sensory ribbon synapses, enabling reliable synaptic information transfer during sustained stimulation. Studies of Ca^{2+}-channel complexes in HEK293 cells indicated that Ca^{2+}-binding proteins (CaBPs) antagonize their calmodulin-dependent inactivation. Although human mutations affecting *CABP2* were shown to cause hearing impairment, the role of CaBP2 in auditory function and the precise disease mechanism remained enigmatic. Here, we disrupted *CaBP2* in mice and showed that CaBP2 is required for sound encoding at inner hair cell synapses, likely by suppressing Ca^{2+}-channel inactivation. We propose that the number of activatable Ca^{2+} channels at the active zone is reduced when CaBP2 is lacking, as is likely the case with the newly described human *CABP2* mutation.

Author contributions: M.M.P. and T.M. designed research; M.M.P., A.G., S.M., A.I., S.J., I.S., A.G.D., R.C., G.V.C., N.S., and T.M. performed research; F.P. contributed new reagents/analytic tools; M.M.P., A.G., S.M., A.I., A.G.D., R.C., N.S., and T.M. analyzed data; and M.M.P., S.J., R.C., G.V.C., N.S., and T.M. wrote the paper.

The authors declare no conflict of interest.

This article is a PNAS Direct Submission.

[1]To whom correspondence may be addressed Email: tmoser@gwdg.de or mm.picher@gmail.com.

This article contains supporting information online at www.pnas.org/lookup/suppl/doi:10.1073/pnas.1617533114/-/DCSupplemental.

contribute to the hearing impairment DFNB93. Moreover, DFNB93 might arise from impaired excitation-secretion coupling due to a depolarized shift of Ca^{2+}-channel activation as was postulated for *CABP4* disruption in photoreceptors in congenital stationary night blindness (36). Finally, CaBP2 reduced the Ca^{2+}-current density in HEK293-T cells, which was not found with the truncated CaBP2 reported to cause DFNB93 (35). Therefore, excess Ca^{2+} influx and glutamate release might cause excitotoxic synapse loss [excitotoxicity during loud noise (37)] in DFNB93.

Here, we describe an unreported human *CABP2* loss-of-function mutation and analyze auditory function of a newly generated *Cabp2*-deficient mouse line at the synaptic, cellular, and systems levels. Lack of Cabp2 enhanced inactivation of Ca^{2+} influx in IHCs, whereas its amplitude and voltage dependence of activation were normal. *Cabp2* deficiency caused reduced and more jittered action potential firing in SGNs and impaired auditory brainstem responses (ABRs) despite intact cochlear amplification. This observation indicates that a synaptic hearing impairment underlies DFNB93.

Results

A Newly Identified Loss-of-Function Mutation in *CABP2* Causes Recessive Hearing Loss. The family (pedigree is shown in Fig. 1*A*) of the affected subjects [a 16-y-old male subject (III:1) and his 11-y-old sister (III:3)] originated from Northern Italy. For the clinical and genetic studies, both parents were also enrolled and all subjects underwent full clinical examinations, excluding syndromic features. Apart from presbyacusis in subjects I:1 and I:4, there was no history of hearing defects in the family. Pedigree reconstruction indicated a common ancestor of the subjects' parents (II:2 and II:5) in the first half of the 19th century. Both affected subjects presented prelingual hearing impairment affecting their communication. Tympanometry indicated normal middle ear function. Pure-tone air conduction audiometry revealed symmetrical moderate-to-severe hearing impairment across all frequencies, preferentially affecting the middle-frequency range ("U shape"; Fig. 1*C*). This feature led to screening for mutations in the *TECTA* and *CABP2* genes, which are known to cause an audiometric phenotype similar the one observed in the subjects (35, 38).

PCR amplification of all seven *CABP2* exons, followed by bidirectional Sanger capillary sequencing, allowed us to identify a homozygous G-to-T transversion at nucleotide 466 in exon 5 (c.466G > T) in the DNA of subject III:1 (Fig. 1*B*, *Top*). The mutation creates a premature stop codon (TAG), likely resulting in a loss of function due to nonsense-mediated mRNA decay (schematic is shown in Fig. 1*D*). The same *CABP2* c.466G > T mutation was found in the homozygous state in the proband's sister (III:3), whereas both parents (II:2 and II:5), the younger unaffected child (III:4), and three other family members (I:1, I:4, and II:4) were carriers of a single copy of the mutated allele (Fig. 1*B*, *Middle*). The presence of the c.466G > T variant was excluded from a sample of 225 control white subjects by restriction analysis of a PCR amplicon encompassing the mutant nucleotide (Fig. 1*B*, *Bottom*). Moreover, there was no G > T sequence variant reported at position 466 in the database of the Exome Aggregation Consortium (exac.broadinstitute.org/). In the four children and their parents, the chromosomal region encompassing the *CABP2* c.466G > T locus was also genotyped for four microsatellites (D11S1765, D11S913, D11S1889, and D11S1337) and four single-nucleotide polymorphisms (rs2256154, rs630172, rs1695, and rs1531514) by capillary electrophoresis of fluorescently labeled PCR amplicons and direct sequencing of PCR

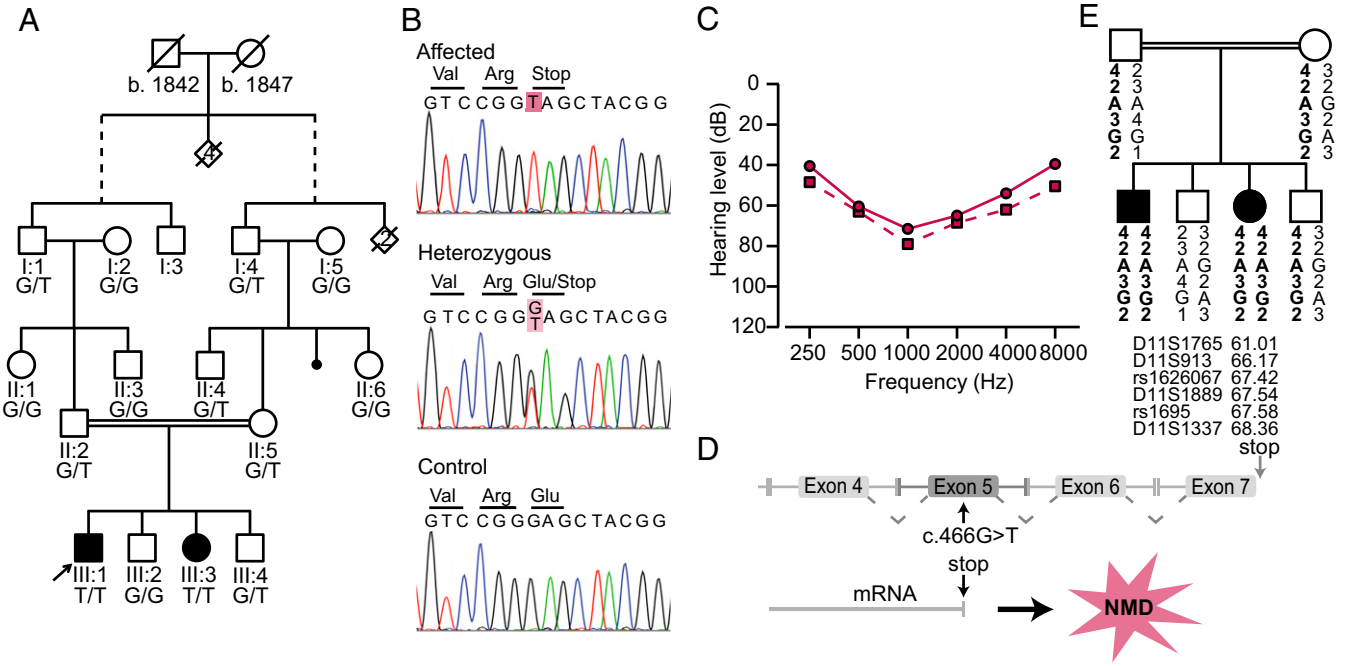

Fig. 1. A previously unidentified mutation in *CABP2* causes moderate-to-severe hearing impairment. (*A*) Pedigree and segregation of the c.466G > T (p.E156X) mutation in a family with hearing-impaired children. Dates of birth (b.) of the common ancestors were ascertained from historical marriage registers and are reported under their symbols. (*B*) Genotyping of test subjects revealed a nonsense mutation in *CABP2*: results of sequencing *CABP2* exon-5 c.460–474 in the proband (subject III:1; *Top*), his father (subject II:2; *Middle*), and one of his unaffected brothers (subject III:2; *Bottom*). Nomenclature is based on NM 016366.2 and NP 057450.2. The mutated nucleotide is highlighted in magenta. Codon 156 is the last one indicated. (*C*) Binaural mean air conduction thresholds of the proband (subject III:1; circles) and his sister (subject III:3; squares). Hearing loss is symmetrical and more pronounced in the middle frequencies. (*D*) Schematic description of *CABP2*, consisting of seven exons, with the c.466G > T mutation indicated by the black arrow. A mutation in exon 5 is predicted to lead to nonsense-mediated decay (NMD). (*E*) Shared haplotype (7.35 Mb) encompassing the c.466G > T transversion in the mutation-bearing paternal and maternal alleles inherited by the children.

products, respectively. Mutation-bearing chromosomes shared a common haplotype (Fig. 1*E*), thus confirming that the pathogenic variant is identical by descent in both parents and has been inherited from a common ancestor, as suggested by pedigree reconstruction.

In conclusion, we identified a mutation in *CABP2* (c.466G > T) that causes a recessive nonsyndromic hearing impairment similar to what we previously described for a splice site mutation in *CABP2*, which is thought to truncate the CaBP2 amino acid sequence. We postulate that both alleles disrupt CaBP2 function and assume that the c.466G > T mutation compromises CaBP2 function via nonsense-mediated mRNA decay. The tone audiograms were comparable between both mutant *CABP2* genotypes (35). However, unlike in our previous report, a transitory evoked otoacoustic emission (TEOAE) was observed in subject III:1 in the course of clinical examination at the age of 4 y (subject III:3 was not tested for TEOAE). This finding suggests that, at least initially, the *CABP2* mutation spared cochlear amplification by outer hair cells (OHCs) and might arise at the level of IHCs in their ribbon synapses or the SGNs. To elucidate the disease mechanism further and study the role of CaBP2 in hearing, we turned to analysis in mice.

Cabp2 Is Expressed in Inner Ear Hair Cells and Is Required for Normal Hearing in Mice. We generated a DFNB93 mouse model by using mouse ES cells of the Knockout Mouse Project (KOMP) repository (CSD50029, DEPD0003_7_F06) that contain an IRES:LacZ trapping cassette in the locus of the *Cabp2* gene, followed by loxP-flanked exons 3 and 4 for Flp- and Cre-mediated conditional deletion (Fig. 2*A*). We derived constitutive $Cabp2^{LacZ/LacZ}$ mutants with globally defective *Cabp2* function by crossing mice carrying the floxed *Cabp2* allele with a Cre-driver line that expresses Cre-recombinase under the promoter of the transcription factor EIIa (39). $Cabp2^{LacZ/LacZ}$ mice were born at Mendelian ratio and were viable and fertile.

First, we studied the expression of *Cabp2* using RT-PCR of the cochlea and LacZ staining of various nervous tissues. Within the cochlea, mRNA for the long Cabp2 isoform was detected in wild-type mice and Cabp2 mRNA was absent in $Cabp2^{LacZ/LacZ}$ mice (Fig. 2*B*). The LacZ signal was restricted to hair cells, with a much stronger staining in IHCs than in OHCs (Fig. 2 *C* and *C′*). In addition, we found LacZ signal in vestibular hair cells (Fig. 2*C″*) and in some cells in the outer retina, potentially representing horizontal cells (Fig. 2*C‴*) because they were positive for calbindin–D-28k (Fig. S1*C*). Sagittal sections of the whole brain appeared to lack LacZ staining (data not shown). Efforts to immunolocalize Cabp2 in IHCs failed with commercially available and newly generated antibodies using various protocols, which resulted in either unspecific staining or lack of staining (data not shown).

Next, we performed recordings of ABRs (reflecting neuronal activity along the early auditory pathway) and of otoacoustic emissions for a first characterization of hearing in $Cabp2^{LacZ/LacZ}$ mice. ABR amplitudes were reduced (Fig. 3*A*) and ABR thresholds were elevated in the frequency range of 6–24 kHz (Fig. 3*B*) in 8-wk-old $Cabp2^{LacZ/LacZ}$ mice of either sex. Heterozygous mice showed normal ABRs (Fig. S1*D*) consistent with the autosomal recessive phenotype observed for human *CABP2* mutations. The thresholds and amplitudes of distortion product otoacoustic emissions (DPOAEs) were comparable between $Cabp2^{LacZ/LacZ}$ mutants and their littermate controls (Fig. 3 *C* and *D*). We probed retinal processing by scotopic electroretinography (ERG), which appeared intact in $Cabp2^{LacZ/LacZ}$ mice (ERGs were not tested at photopic conditions). In summary, within the ear, Cabp2 is expressed in IHCs, OHCs, and vestibular hair cells but not in cochlear spiral ganglion neurons. Based on this expression pattern and our recordings of ABRs and DPOAEs, we hypothesize that the impairment of auditory processing occurs downstream of hair cell mechanoelectrical transduction and OHC amplification, most likely at the IHC synapses, a condition also known as auditory synaptopathy (40).

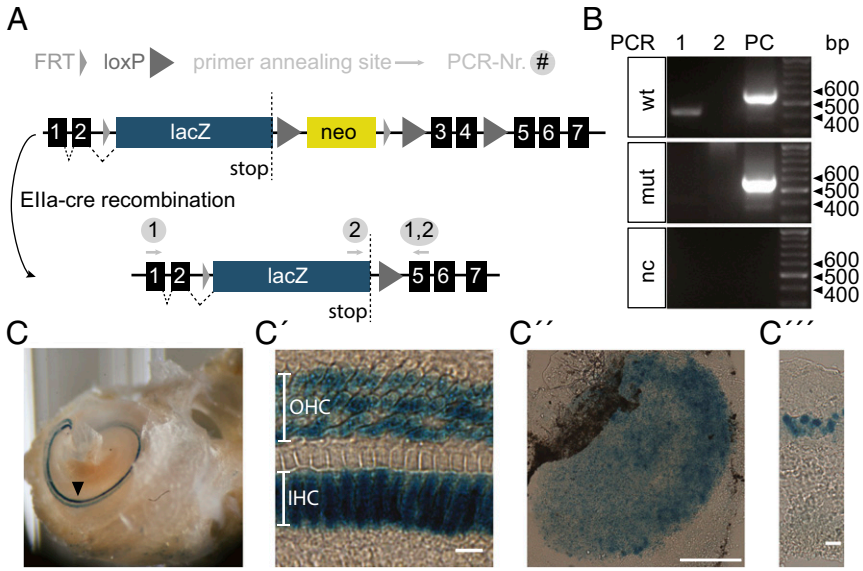

Fig. 2. Cabp2 is expressed in hair cells of the inner ear and in the retina. (*A*) Schematic of IRES:LacZ *Cabp2* trapping cassette with loxP sites flanking the neomycin resistance and exons 3 and 4 of *Cabp2*. Exon 2 is not expressed in the short Cabp2 isoform. EIIa-cre recombination induces the removal of the neomycin cassette and critical exons, resulting in a LacZ-tagged null allele. RT-PCR primer (Table S1) annealing sequences are shown by gray arrows and are provided with the respective PCR number (Nr.) they were used for. (*B*) RT-PCR of the apical turn of the organ of Corti comparing Cabp2 mRNA expression in $Cabp2^{+/+}$ and $Cabp2^{LacZ/LacZ}$ mice, respectively. Primer annealing regions are located in exon 1 and exon 5 (PCR1, positive in $Cabp2^{+/+}$) or in the LacZ sequence and exon 5 (PCR2: negative upon *Cabp2* deletion). In $Cabp2^{+/+}$, one band at 418 base pairs (bp) was identified, confirming the expression of the long-CaBP2 isoform in the organ of Corti. The absence of a band in PCR1 and PCR2 of $Cabp2^{LacZ/LacZ}$ tissue confirms the truncation of *Cabp2* ($n = 3$ animals). GAPDH was used as a positive control (PC; 572 bp) mut, $Cabp2^{LacZ/LacZ}$; nc, negative control (water). (*C*) β-Galactosidase staining of the cochlea, utricle, and retina of $Cabp2^{LacZ/LacZ}$ mice is shown. IHCs, OHCs (*C* and *C′*) and vestibular hair cells (*C″*) were LacZ-positive. (Scale bars: *C′*, 20 μm; *C″*, 500 μm.) (*C‴*) In retinal slices, the LacZ signal was detected in the inner nuclear layer. (Scale bar: 20 μm.)

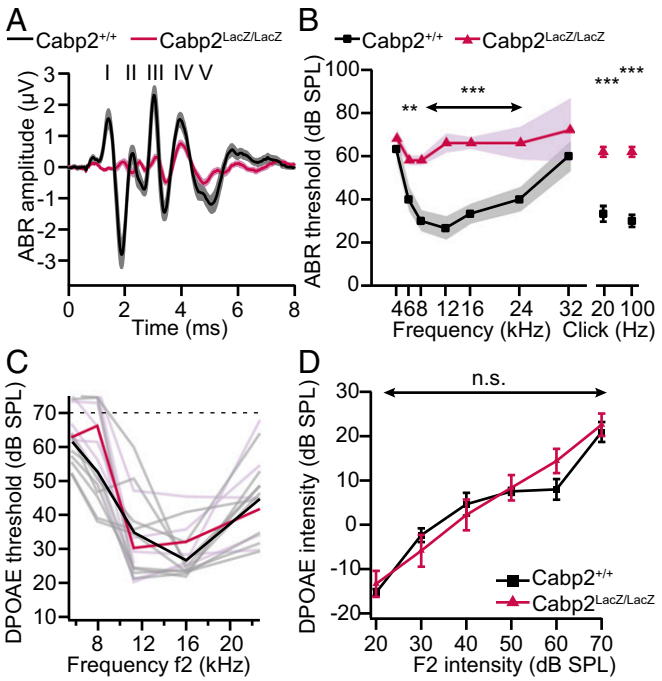

Fig. 3. Synaptic hearing impairment in *Cabp2*$^{LacZ/LacZ}$ mice. (*A*) Grand averages (lines) and SEMs (shaded areas) of ABR waveform responses to 80-dB click stimuli at a stimulus rate of 20 Hz in *Cabp2*$^{+/+}$ ($n = 9$) and *Cabp2*$^{LacZ/LacZ}$ ($n = 7$) mice at P49–P63. Roman numerals on top of the ABR graph denote the Jewett ABR waves. Note the decrease in amplitude and delay of wave I in *Cabp2*-deficient mice compared with *Cabp2*$^{+/+}$ mice. (*B*) Elevated ABR thresholds in P49–P63 mice. Tone bursts are presented at a stimulus rate of 40 Hz and clicks at 20 or 100 Hz. Error bars represent SEM, and *P* values are indicated with asterisks (**$P < 0.01$, ***$P < 0.001$; Holm–Sidak *t* test) and 20- and 100-Hz click stimuli (***$P < 0.001$, Holm–Sidak *t* test). (*C*) DPOAE thresholds (defined as the interpolated f2 intensity required to elicit a DPOAE of 10-dB SPL) for *Cabp2*$^{LacZ/LacZ}$ (seven individual traces shown in purple, mean shown in magenta) and *Cabp2*$^{+/+}$ (nine individuals shown in gray, mean shown in black) mice. The dashed line indicates the maximum loudspeaker output of 70 dB. DPOAE thresholds were comparable between genotypes ($P > 0.05$, two-way ANOVA). (*D*) Mean DPOAE growth functions for *Cabp2*$^{LacZ/LacZ}$ ($n = 8$) and *Cabp2*$^{+/+}$ ($n = 9$) mice at f1 = 9.4 kHz and f2 = 11.3 kHz are shown. DPOAEs were comparable between both genotypes at the age of 8 wk, indicating intact active cochlear amplification in *Cabp2*-deficient mice ($P > 0.05$, two-way ANOVA). Error bars represent SEM. n.s., $P > 0.05$.

***Cabp2* Disruption Does Not Alter the Number and Gross Molecular Anatomy of IHCs and Their Afferent Synapses.** We studied the number and gross morphology of IHCs and their afferent synapses using confocal microscopy of immunolabeled organs of Corti. Using parvalbumin-α or Ctbp2/RIBEYE as a hair cell marker, we did not find an obvious IHC loss in *Cabp2*$^{LacZ/LacZ}$ mice at the age of 2–3 and 8 wk (Fig. S2). The development of IHCs appeared unaffected, as tested by staining of small- and large-conductance Ca^{2+}-activated K^+ channels (SK and BK, respectively) after the onset of hearing (Fig. S2 *A* and *B*). As expected for normal postnatal IHC maturation, BK channels were located at the neck region of IHCs and SK2 puncta were absent in IHCs (but present in OHCs) of *Cabp2*$^{LacZ/LacZ}$ mice at postnatal day 15 (P15; Fig. S2*B*). The number of ribbon-occupied synapses, identified as juxtaposed spots of CtBP2/RIBEYE (marking the presynaptic ribbon) and GluA2/3 (marking the postsynaptic glutamate receptor clusters) immunofluorescence (41), as well as the total number of synapses (GluA2/3 spots), were indistinguishable between *Cabp2*$^{LacZ/LacZ}$ mutants and littermate controls at 3 and 8 wk of age (Fig. S2 *C–E*). This observation rules out the possibility that DFNB93 was caused by a loss of IHCs or their synapses (e.g., due to degeneration or glutamate excitotoxicity). Moreover, immunolabeling for $Ca_V1.3$ and CtBP2/RIBEYE indicated normal synaptic clustering of IHC Ca^{2+} channels in 8-wk-old *Cabp2*$^{LacZ/LacZ}$ mutants (Fig. S2*F*). In summary, *Cabp2* disruption does not affect the maturation, number, or gross molecular anatomy of IHCs and their afferent synapses.

Disruption of *Cabp2* Causes Enhanced Ca^{2+}-Current Inactivation. Next, we revisited the regulation of IHC-like $Ca_V1.3$ channels by CABP2 in HEK293 cells using a refined approach [corrected $Ca_V1.3\alpha$ clone (22) and improved cell viability by coexpression of a Ca^{2+}-activated K^+ channel (SK3-1) limiting Ca^{2+} influx at the resting potential]. We found comparable maximal current densities [Ca^{2+} currents normalized to the cell capacitance in picoampere per picofarad (pA/pF)] in the presence or absence of CABP2 [Fig. S3*A*; −87.47 ± 20.04 pA/pF with CABP2 vs. −57.45 ± 12.09 pA/pF without CABP2 (control); $P > 0.05$, Wilcoxon rank sum test]. This observation contrasts with our previous report of a reduction in current density when coexpressing CABP2 in HEK293-T cells (35), which might reflect a selection bias related to cell viability issues due to the noninactivating Ca^{2+} influx in the absence of a negative feedback. Moreover, we observed that CABP2 shifted the voltage dependence of $Ca_V1.3$ activation to more hyperpolarized potentials [Fig. S3*B*; potential of half-activation ($V_{0.5}$) of −35.4 ± 1.5 mV compared with $Ca_V1.3$ alone: −20.8 ± 1.1; $P < 0.001$, Student's *t* test] as previously reported for $Ca_V1.4$ (36). This observation primarily reflected an increased voltage sensitivity, because the slope factor of the activation function (k_{act}) was significantly smaller when coexpressing CABP2 (Fig. S3*B*; $P < 0.005$, Student's *t* test). Under these recording conditions, we confirmed the potency of CABP2 to inhibit $Ca_V1.3$ Ca^{2+}-current inactivation (35) (Fig. S3 *C–E*).

Next, we performed perforated-patch recordings of whole-cell Ca^{2+} currents in IHCs of *Cabp2*$^{LacZ/LacZ}$ mice to address our two key hypotheses on Cabp2 function in regulating IHC Ca^{2+} current: (*i*) hyperpolarized shift of Ca^{2+}-channel activation out of the physiological range of receptor potentials (36) and (*ii*) inhibition of Ca^{2+}-channel inactivation. We studied mature IHCs of the apical coil of the cochlea at 5 wk of age. For comparison with our in vivo experiments, we aimed to match the physiological conditions most closely by performing perforated-patch recordings at 37 °C and at an extracellular Ca^{2+} concentration ($[Ca^{2+}]_e$) of 1.3 mM. Ca^{2+} currents of *Cabp2*$^{LacZ/LacZ}$ IHCs elicited by depolarizations (20 ms to various potentials) were normal in amplitude, at least when probed from a holding potential of −57 mV (Fig. 4 *A* and *B*), which is compatible with a normal total number of Ca^{2+} channels.

Moreover, the voltage dependence of Ca^{2+} influx (Fig. 4*B*) and fractional Ca^{2+}-channel activation (Fig. 4*C*) were comparable in IHCs with and without functional CaBP2. Both the voltage of half-maximal Ca^{2+}-channel activation ($V_{0.5}$: −28.03 ± 0.85 mV for *Cabp2*$^{LacZ/LacZ}$ vs. −27.72 ± 0.94 mV for *Cabp2*$^{+/+}$; $P > 0.05$, Student's *t* test) and k_{act} (7.07 ± 0.08 mV for *Cabp2*$^{LacZ/LacZ}$ vs. 7.41 ± 0.12 mV for *Cabp2*$^{+/+}$; $P > 0.05$, Student's *t* test) were statistically indistinguishable. These observations indicate that CaBP2 regulation of $Ca_V1.3$ is dispensable for the voltage dependence of IHC Ca^{2+} influx and argue against a deficit of excitation-secretion coupling due to a depolarized shift of the voltage range of $Ca_V1.3$ operation as a disease mechanism of DFNB93. Activation (Fig. 4*D*) and deactivation (Fig. 4*E*) kinetics were unaltered in *Cabp2*$^{LacZ/LacZ}$ IHCs (time constant of voltage-clamp of ∼160 μs, average series resistance of 17.8 MΩ for perforated-patch recordings at physiological temperature).

Using long (500 ms) step depolarizations to −14 mV and comparing residual Ca^{2+} currents at 500 ms ($I_{500,Ca}$; Fig. 4 *F* and *G*) or trains of brief depolarizations (10 ms to −14 mV, 5-ms interval; Fig. 4*H*) we found $Ca_V1.3$ inactivation to be substantially increased in *Cabp2*$^{LacZ/LacZ}$ IHCs. Both the fast exponential

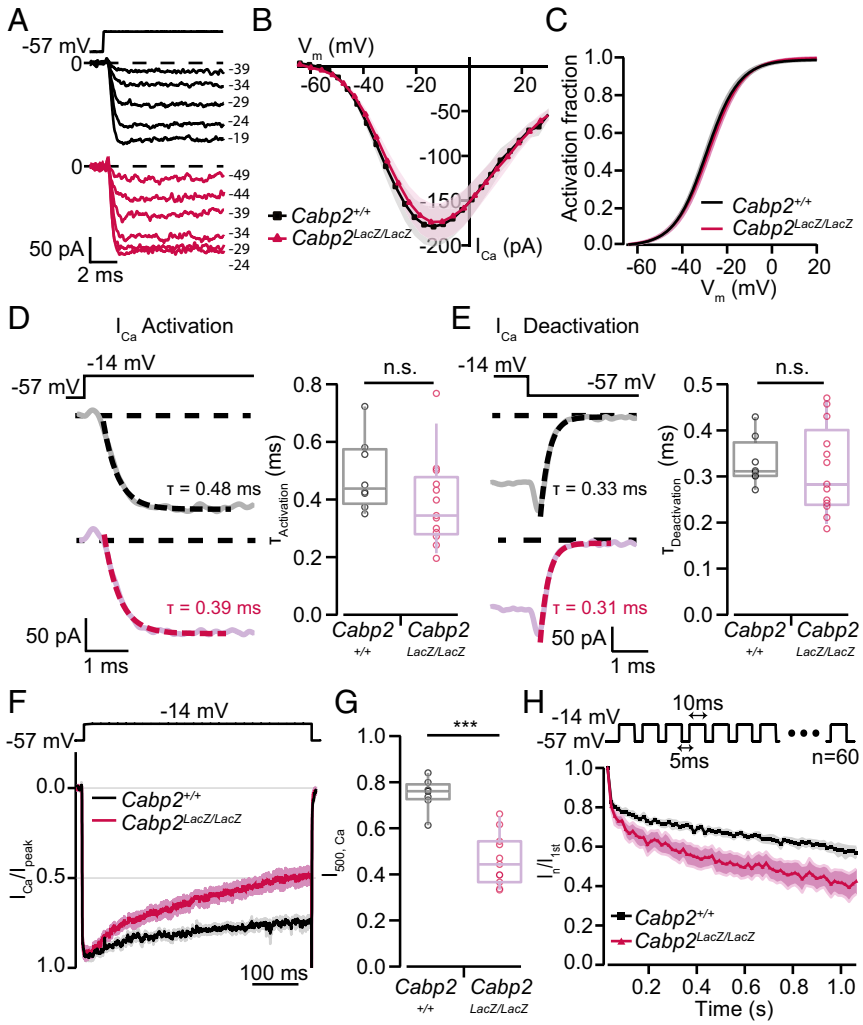

Fig. 4. Enhanced Ca^{2+}-current inactivation in *Cabp2*-deficient IHCs of 5-wk-old mice recorded in near-physiological conditions. (*A*) Representative Ca^{2+}-current traces of $Cabp2^{+/+}$ (*Top*) and $Cabp2^{LacZ/LacZ}$ (*Bottom*) IHCs of P39 and P44 animals. (*B*) Comparable current–voltage (I-V) relationships of $Cabp2^{+/+}$ ($n = 8$) and $Cabp2^{LacZ/LacZ}$ ($n = 11$) IHCs. Traces are depicted as mean ± SEM (shaded area). V_m, membrane potential. (*C*) Average activation curve derived from *B* shows comparable voltage dependence of activation between both genotypes (mean ± SEM). (*D*, *Left*) Experimental paradigm and representative Ca^{2+}-current (I_{Ca}) traces of $Cabp2^{+/+}$ (*Top*) and $Cabp2^{LacZ/LacZ}$ (*Bottom*) IHCs overlaid by exponential fit to determine activation kinetics. (*D*, *Right*) Quantification of activation time ($T_{activation}$) constants showing comparable results for $Cabp2^{LacZ/LacZ}$ and $Cabp2^{+/+}$ IHCs (Wilcoxon rank sum test). (*E*, *Left*) Experimental paradigm and representative Ca^{2+}-current traces of $Cabp2^{+/+}$ (*Top*) and $Cabp2^{LacZ/LacZ}$ (*Bottom*) IHCs overlaid by an exponential fit to determine deactivation kinetics. (*E*, *Right*) Quantification of deactivation time constants showing comparable results for $Cabp2^{LacZ/LacZ}$ and $Cabp2^{+/+}$ IHCs (Student's *t* test). n.s., no significant difference. (*F*) Experimental paradigm and Ca^{2+} currents recorded from $Cabp2^{+/+}$ ($n = 8$) and $Cabp2^{LacZ/LacZ}$ ($n = 11$) IHCs at near-physiological conditions [35–37 °C, 1.3 mM Ca^{2+}, holding potential (V_h) = −57 mV]. I_{peak}, peak current. Traces are presented as mean ± SEM. (*G*) Quantification of residual Ca^{2+} currents at 500 ms ($I_{500,Ca}$) shows enhanced inactivation in *Cabp2*-deficient compared with $Cabp2^{+/+}$ IHCs (***$P < 0.001$, Student's *t* test). (*H*) Progression of inactivation during train stimulation of $Cabp2^{LacZ/LacZ}$ ($n = 14$) and $Cabp2^{+/+}$ ($n = 14$) IHCs. Note the increase of inactivation with ongoing stimulation in $Cabp2^{LacZ/LacZ}$ IHCs ($P < 0.005$, Student's *t* test). I_{1st}, current evoked by first depolarization; I_n, current evoked by *n*'s depolarization. Throughout the article, box plots and overlaid individual data points are presented. Box plots show the median as a horizontal line flanked by quartiles, and whiskers are presented as the 1.5-interquartile range from box edges.

(amplitude: 0.217 ± 0.027 for $Cabp2^{LacZ/LacZ}$ vs. 0.114 ± 0.028 for $Cabp2^{+/+}$; $P < 0.05$, Student's *t* test) and the slower linear (slope: 0.607 ± 0.011 for $Cabp2^{LacZ/LacZ}$ vs. 0.257 ± 0.040 for $Cabp2^{+/+}$; $P < 0.01$, Student's *t* test) components of $Ca_V1.3$ inactivation were increased, whereas the time constant of the fast component was unaltered ($\tau_{inactivation}$: 38.3 ± 6.9 ms for $Cabp2^{LacZ/LacZ}$ vs. 39.3 ± 7 ms for $Cabp2^{+/+}$).

To gain further insight into the type of inactivation, we also studied IHCs of 2- to 3-wk-old $Cabp2^{LacZ/LacZ}$ mice at room temperature for easier manipulation of the preparation. We chose midcochlear IHCs because the ABR impairment was most evident in the range of 12–16 kHz at this age (Fig. S4 *A* and *B*). Using long depolarizations (500 ms to −14 mV; Fig. S4*C*) or trains of brief depolarizations (10 ms to −14 mV, 5-ms interval; Fig. S4*F*), we observed a modest but significant increase in $Ca_V1.3$ inactivation in $Cabp2^{LacZ/LacZ}$ IHCs ($I_{500,Ca}$:0.62 ± 0.03 for $Cabp2^{LacZ/LacZ}$ vs. 0.73 ± 0.01 for $Cabp2^{+/+}$; $P < 0.001$, Student's *t* test). Interestingly, the enhanced $Ca_V1.3$ inactivation in mutant IHCs primarily represented more voltage-dependent inactivation (VDI), as demonstrated by residual Ba^{2+} currents after 500 ms ($I_{500,Ba}$: 0.71 ± 0.02 for $Cabp2^{LacZ/LacZ}$ vs. 0.78 ± 0.01 for $Cabp2^{+/+}$; $P < 0.005$, Student's *t* test; Fig. S4 *D* and *E*). In addition, there was a trend toward increased CDI, calculated as the difference between residual Ba^{2+} and Ca^{2+} currents after 500 ms, which, however, did not reach statistical significance ($P > 0.05$, Wilcoxon rank sum test; Fig. S4*E*). Although the data on $Ca_V1.3$ in *Cabp2*-deficient IHCs and in CABP2-expressing HEK293 cells jointly argue for inhibition of $Ca_V1.3$ inactivation by CaBP2 (Fig. 4 *F*–*H*

vs. Fig. S3 *C–E*), they disagree about regulation of the voltage dependence of Ca^{2+}-channel activation. We conclude that the heterologous expression system reconstitutes the regulation of $Ca_V1.3$ by CaBP2 in IHCs only partially.

Assessing Ca^{2+}-induced exocytosis by perforated-patch membrane capacitance measurements did not reveal a reduction of exocytosis. In fact, we observed enhanced capacitance increments for long depolarizations (5-wk-old animals: $P < 0.001$ for 100 and 200 ms, Student's *t* test; Fig. S5 *A* and *B*). This excess exocytosis was prevented after the coapplication of the synthetic Ca^{2+} chelators ethylene glycol-bis(β-aminoethyl ether)-*N*,*N*,*N*′,*N*′-tetraacetic acid (EGTA) and 1,2-bis(*o*-aminophenoxy)ethane-*N*,*N*,*N*′,*N*′-tetraacetic acid (BAPTA) in a ruptured-patch configuration (Fig. S5*C*) at concentrations (0.5 mM each) that were previously approximately found to mimic the action of endogenous Ca^{2+} buffers in IHCs (42). The excess of sustained IHC exocytosis in Cabp2-deficient mice might indicate a contribution of CaBP2 in Ca^{2+} buffering at the active zone. To test Ca^{2+} buffering properties of CaBP2 further, we used isothermal titration calorimetry and identified two Ca^{2+} binding sites in wild-type CaBP2 that seem compatible with low-affinity Ca^{2+} buffering by CaBP2 (Fig. S6 and Table S2). Lack of Ca^{2+} buffering by CaBP2 might enable wider Ca^{2+} spread, promoting extrasynaptic exocytosis. Such a scenario has been proposed as an explanation for excessive sustained exocytosis in triple EF-hand, Ca^{2+}-buffer KO mice (42). In summary, we found normal activation and deactivation but increased inactivation of $Ca_V1.3$ Ca^{2+} currents in *Cabp2*-deficient IHCs.

Disruption of *Cabp2* Impairs Synaptic Sound Encoding. One way to probe synaptic release largely independent from potential extrasynaptic exocytosis is to record the sound-evoked spiking of single SGNs, each of which is thought to be driven by a single active zone (42). Therefore, and to analyze how *Cabp2* deficiency affects synaptic sound encoding, we performed in vivo extracellular recordings from single SGNs where they enter the cochlear nucleus (43). Spontaneous firing rates were reduced in $Cabp2^{LacZ/LacZ}$ mice at the age of 5–8 wk (Fig. 5*A*; $P < 0.001$, pooling littermates and C57BL/6 controls). We then studied sound encoding by measuring SGN firing upon tone-burst stimulation. We found frequency tuning and spike rate thresholds ($P = 0.21$, for fibers with characteristic frequencies of 6–20 kHz) to be normal in SGNs of $Cabp2^{LacZ/LacZ}$ mice (Fig. S7 *A* and *B*). This observation corroborates our notion of normal cochlear amplification (DPOAE; Fig. 3 *C* and *D*). We recorded rate-level functions [firing rate vs. sound pressure level (SPL)] in response to tone bursts of different SPLs at the characteristic frequency (50 ms, applied at 5 Hz; Fig. S7*C*). Neither the dynamic range of encoding nor the steepness of the rate-level functions was altered in $Cabp2^{LacZ/LacZ}$ SGNs (Fig. S7 *D* and *E*). However, when studying maximal firing by tone bursts at saturating sound–

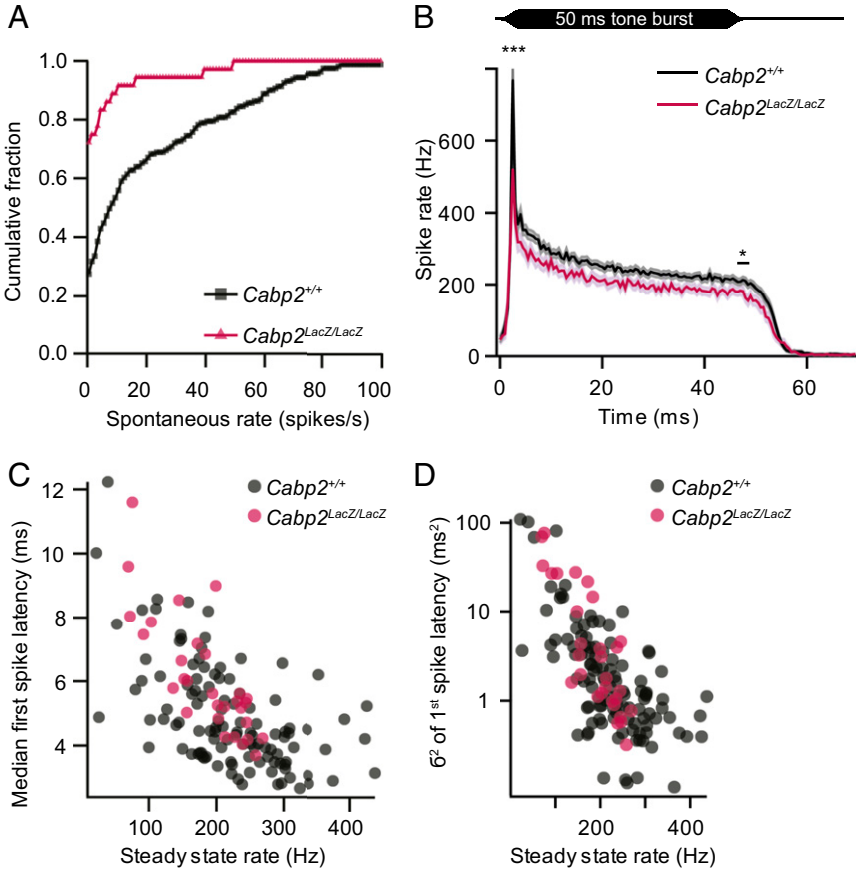

Fig. 5. Cabp2 is required for normal spontaneous and sound-evoked firing of SGNs. (*A*) Cumulative plot of spontaneous firing rates of SGNs recorded from $Cabp2^{LacZ/LacZ}$ ($n = 36$) and $Cabp2^{+/+}$ SGNs ($n = 161$, pooling littermate controls and C57Bl6 controls). Note the higher fraction of low spontaneous rate fibers in $Cabp2^{LacZ/LacZ}$ mice ($P < 0.001$, Kolmogorov–Smirnov test). (*B*) Peak-aligned grand averages of poststimulus time histograms of SGNs (bin width = 0.5 ms) recorded in response to 200 50-ms tone bursts. The time course of adaptation of $Cabp2^{LacZ/LacZ}$ SGNs ($n = 30$) is comparable to $Cabp2^{+/+}$ SGNs ($n = 112$, pooling littermates and C57Bl6 controls). $*P < 0.05$, $***P < 0.005$. (*C*) Summary of first-spike latencies of SGNs (scattered against steady-state firing rate) showing delayed responses in $Cabp2^{LacZ/LacZ}$ compared with $Cabp2^{+/+}$ animals ($P < 0.001$, Wilcoxon rank sum test). (*D*) Variance (6^2) of the first-spike latency (scattered against steady-state firing rate). Variance is increased in SGNs of *Cabp2*-deficient compared with $Cabp2^{+/+}$ animals ($P < 0.05$, Wilcoxon rank sum test).

pressure levels (50 ms, applied at 5 Hz, 30 dB above threshold at the characteristic frequency), we found reduced firing rates at sound onset and after short-term adaptation in $Cabp2^{LacZ/LacZ}$ SGNs (Fig. 5*B*). Congruent with the reduction in firing rates, first-spike latencies were delayed (Fig. 5*C*; 6.1 ± 0.3 ms vs. 4.9 ± 0.2 ms) and more variable (Fig. 5*D*; variance: 11.5 ± 3.6 ms^2 vs. 6.0 ± 1.5 ms^2) in $Cabp2^{LacZ/LacZ}$ SGNs. Rate reduction and increased jitter of SGN firing at sound onset likely explain the impaired ABR wave I amplitude and threshold.

The reduction in firing rates was also observed when using 500-ms tone bursts (applied at 0.5 Hz; Fig. S6*F*). Here, adaptation was slightly more pronounced in $Cabp2^{LacZ/LacZ}$ SGNs (36.4% vs. 20.5% reduction between 40–50 ms and 490–500 ms after stimulus onset). Interestingly, there was no increase of spike rate after short-term adaptation as would have been expected if the excess-sustained exocytosis observed in *Cabp2*-deficient IHCs reflected enhanced synaptic release. Therefore, such excess-sustained exocytosis likely occurs extrasynaptically and does not contribute to sound encoding, much like the suggested scenario for mice lacking the EF-hand calcium-binding proteins calbindin–D-28k, calretinin, and parvalbumin-α (42).

Discussion

Here, we studied the role of CaBP2 in hearing and characterized the disease mechanism of human sensorineural hearing impairment DFNB93. We identified a DFNB93 mutation that likely causes a complete loss of *CABP2* function. Using constitutive genetic disruption of *Cabp2*, we generated a DFNB93 mouse model that showed a synaptic hearing impairment without loss of IHCs or their synapses with SGNs. We did not observe obvious deficits outside the auditory system, which is in keeping with the rather hair cell-specific expression of CaBP2 and the clinical findings in DFNB93 (this study and refs. 35, 44). Elevated thresholds, reduced amplitudes and prolonged latencies of ABRs, of which the first peak reports the synchronous activation of SGNs, are likely accounted by the reduced firing rates and delayed, as well as more variable, spike timing of SGNs at sound onset. We propose that reduced firing of SGNs in $Cabp2^{LacZ/LacZ}$ mice results from enhanced steady-state inactivation of $Ca_V1.3$ at the IHC active zone in vivo, reducing the number of Ca^{2+} channels available for triggering synaptic vesicle release.

Regulation of IHC $Ca_V1.3$ Channels by CaBP2. IHC $Ca_V1.3$ Ca^{2+} channels stand out by reason of their hyperpolarized activation range and modest inactivation (10, 18, 19, 22, 45). These properties have been attributed to the molecular composition of the native Ca^{2+}-channel complexes that, in addition to the specific pore-forming $Ca_V1.3α1$ splice variant (46), auxiliary $Ca_Vβ2$ (6, 47), and $Ca_Vα_2δ2$ (7) subunit, also contain interactions partners, such as Rab3-interacting molecule (RIM) (48, 49); harmonin (50, 51); calmodulin; and, notably, CaBPs (this study and refs. 18, 19, 34). CaBPs have been shown to confer both the negative activation (36) and the noninactivating (18, 19, 35, 52) phenotypes to Ca_V channels in HEK293 cells. Our HEK293 cell study demonstrates that CaBP2 can potently shift $Ca_V1.3$ activation to more hyperpolarized potentials and inhibit $Ca_V1.3$ channel inactivation. Aiming to match the molecular composition of the IHC $Ca_V1.3$ channel complex closely and using coexpression of SK3-1 channels for avoiding potentially toxic Ca^{2+} influx, we did not observe the previously reported decrease of Ca^{2+}-current density upon CABP2 coexpression (35).

$Cabp2^{LacZ/LacZ}$ mice allowed us to confirm expression of CaBP2 in IHCs and OHCs (18, 34) with high specificity due to use of a genetic marker. The function of CaBP2 in OHCs remains elusive. Due to the predominant expression of $Ca_V1.3_{ΔIQ}$ in OHCs [a splice variant that is lacking the C-terminal CaBP2-binding isoleucine/glutamine motif (IQ motif) region and CDI (53)], CaBP2 is probably not required for Ca^{2+}-channel regulation in OHCs. Alternatively, CaBP2 might contribute to Ca^{2+} buffering also in OHCs. However, quantitative estimates of EF-hand Ca^{2+}-buffer concentrations proposed 5-mM Ca^{2+} binding sites provided by calbindin–D-28k and oncomodulin (31). Moreover, OHC electromotility is critically dependent on oncomodulin (54), whereas disruption of CaBP2 did not affect cochlear amplification. Therefore, CaBP2 likely only plays a minor role in Ca^{2+} buffering in OHCs.

Using $Cabp2^{LacZ/LacZ}$ mice, we tested the three hypotheses of CaBP2 action on $Ca_V1.3$ channels in IHCs: (*i*) reducing Ca^{2+}-current amplitude, (*ii*) hyperpolarized shift of activation, and (*iii*) inhibiting inactivation. Our results could reject the former two hypotheses: Ca^{2+}-current density in IHCs (*i*) and voltage dependence of activation (*ii*) were unchanged. Ca^{2+}-current inactivation (*iii*), on the other hand, was nearly doubled when probing *Cabp2*-deficient IHCs of 5-wk-old mice at near-physiological conditions (Fig. 4), supporting the hypothesis that CaBP2 inhibits the inactivation of $Ca_V1.3$ Ca^{2+} channels in IHCs in vivo. We note that Ca^{2+}-current inactivation was previously shown to be temperature-dependent in IHCs of rats (16), likely explaining why we observed a smaller increase of inactivation at room temperature (Fig. S4). There, we found significantly increased VDI and a nonsignificant trend toward increased CDI in IHCs of 2- to 3-wk-old $Cabp2^{LacZ/LacZ}$ mice. A dual role in Ca^{2+}-channel regulation was hypothesized for CaBP1: The N-lobe/linker regions were suggested to introduce Ca^{2+}-dependent facilitation of $Ca_V1.2$ channels, whereas the C-terminal domains were required for the binding of CaBP1 to the IQ domain and inhibition of $Ca_V1.2$ CDI (55, 56). CaBP1 and CaBP2 share the N-terminal myristoylation as a common modification (27) and, unlike CaBP4 and CaBP5, were implicated in inhibiting VDI of $Ca_V1.3$ channels (18), suggesting that CaBP2 might regulate VDI via the N-lobe region. During VDI, the alpha interaction domain (AID) of $Ca_V1.3α1$ was shown to play a critical role (57), whereby the "lid" ($Ca_Vβ$–AID complex) is thought to mediate VDI by binding segment 6 of $Ca_V1.3α1$, occluding the channel pore (58). Hence, CaBP2 might attenuate VDI by shielding the Ca^{2+}-channel pore from the $Ca_Vβ$–AID complex. Aside from inhibition by CaBP2, $Ca_V1.3$ inactivation is also controlled by the C-terminal regulating domain present or absent depending on the precise $Ca_V1.3$ splice variant (20, 46); by the $Ca_Vβ$ subunit (6); and by interacting proteins, such as other CaBPs (18, 19) and RIM (48).

Considering a biological system as complex as the auditory pathway with limited potential for molecular manipulation, it seems well-justified to characterize function and regulation of IHC-like $Ca_V1.3$ channels in a "simple" heterologous expression system, such as HEK293 cells. However, the differences found here clearly indicate the limitations of a heterologous expression system to represent the physiology of the native IHC Ca^{2+} channels, likely because it has not fully recapitulated the molecular machinery constituting the presynaptic $Ca_V1.3$ Ca^{2+}-channel complex at the IHC active zone. Future studies in mice combining CaBP2 disruption with disruption of CaBP 1, CaBP4, and CaPB5, which are also expressed in IHCs (18, 19, 34), will be important to comprehend the complex regulation of inactivation of IHC Ca^{2+} channels.

Analysis of *Cabp2*-Deficient Mice Indicates That DFNB93 Is an Auditory Synaptopathy. The constitutive disruption of *Cabp2* in mice likely provides an appropriate model for at least some cases of DFNB93, such as for the newly identified *CABP2* mutation, which probably causes nonsense-mediated decay of *Cabp2*-mRNA. Hearing loss characterized by impaired ABR despite intact cochlear amplification as found in $Cabp2^{LacZ/LacZ}$ mice is termed "auditory neuropathy" or "auditory synaptopathy," depending on the site of lesion (40, 59). In keeping with this hypothesis, we observed otoacoustic emissions in one of the DFNB93 subjects described in the present study. As reported for otoferlin-related synaptopathy, emissions might be lost secondarily (60),

potentially explaining the absence in our previous study (35). Lack of CaBP2 expression in SGNs and the normal presence of IHCs and their afferent synapses with SGNs indicated that the hearing deficit in *Cabp2*$^{LacZ/LacZ}$ mice resulted from a dysfunction of the presynaptic active zone. Congruent with previous reports on DFNB93 (35, 44), low to middle frequencies were most affected in human patients, suggesting that inhibition of Ca^{2+}-current inactivation is predominantly required for normal perception of low- to middle-frequency sounds. In fact, in low-frequency hearing animals like bullfrogs, Ca^{2+}-current inactivation was absent during sine-wave stimulation, supporting temporally precise glutamate release and phase-locked excitatory postsynaptic currents (61). Future genetic manipulation in low-frequency hearing gerbils will be beneficial for our understanding of how Ca^{2+}-current inactivation relates to the temporal precision of sound encoding.

In vivo postsynaptic recordings from SGNs revealed reduced rates of spontaneous and evoked synaptic transmission. Our analysis of *Cabp2*-deficient mouse IHCs indicated that the voltage dependence of IHC Ca^{2+} influx was unaltered, ruling out a mismatch of the operating range of $Ca_V1.3$ channels and IHC receptor potentials, respectively, as a disease mechanism for DFNB93. These observations leave enhanced $Ca_V1.3$ inactivation as a plausible candidate mechanism for the reduced rates of transmission at the IHC synapses of *Cabp2*$^{LacZ/LacZ}$ mice and for the human hearing impairment DFNB93. The reduction in spontaneous SGN firing observed in *Cabp2*$^{LacZ/LacZ}$ mice suggests that some of the $Ca_V1.3$ channels are inactivated at the resting potential upon *Cabp2* deficiency, because spontaneous firing depends on the opening of Ca^{2+} channels (13). Interestingly, unlike what is expected from findings in the normal cochlea, where SGNs with low spontaneous rates tend to display higher thresholds (43), we found SGNs that combined low spontaneous rates with low thresholds in *Cabp2*$^{LacZ/LacZ}$ mice and thresholds were generally comparable to wild-type SGNs. We argue that impaired sound coding, also encompassing reduced temporal precision, characterizes the hearing impairment of human DFNB93 subjects.

We postulate that inactivation within the relatively depolarized operating range of IHCs (11, 12) reduces the number of synaptic $Ca_V1.3$ channels available for stimulus-secretion coupling in the absence of CaBP2. Membrane capacitance (C_m) measurements turned out to be of limited help for understanding the effect of CaBP2 disruption on synaptic exocytosis. An enhanced spread of the synaptic Ca^{2+} signal to extrasynaptic release sites might account for excess sustained vesicle fusion, which possibly masked a reduction of synaptic exocytosis underlying the reduced SGN spike rates. Based on the normal sound-evoked firing of SGNs of mice lacking the EF-hand Ca^{2+} buffers calbindin–D-28k, calretinin, and parvalbumin-α, we assume that the proposed impaired Ca^{2+} buffering in CaBP2-deficient IHCs does not contribute to the sound coding deficit in *Cabp2*$^{LacZ/LacZ}$ mice. Imaging synaptic Ca^{2+} signals in CaBP2-deficient IHCs, as well as studying mice with IHC-specific *Cabp2* deletion and virus-mediated rescue of CaBP2 function in IHCs, will be required to validate the $Ca_V1.3$ inactivation hypothesis of DFNB93 pathophysiology further.

Materials and Methods

Generation of the *Cabp2*$^{LacZ/LacZ}$ Mouse Line. ES cells carrying the KO allele were provided by the KOMP repository, and the methods used were previously described (62). The sequence integrity and the presence of the distal loxP cassette, together with the correct insertion of the targeted allele, were confirmed by long-range PCR assay of ES cell clones and subsequent sequencing according to the manufacturer's protocol (Fig. S1 *A* and *B*). Primers used can be found on the KOMP web page. The primer pair to check insertion of the 3′ target allele is fwd3′ allele and rev3′ allele (primer list is provided in Table S1). The mutant mice were crossbred with Ella-cre transgenic mice, resulting in a global Cabp2 mutant mouse line carrying a LacZ reporter after exon 2 of Cabp2. Mice of either sex were used at P14–P21, P35–P42, and P49–P62 for patch-clamping and immunohistochemistry, and at 3–8 wk for systems physiology. All experiments were performed in compliance with the national animal care guidelines and were approved by the Board for Animal Welfare of the University Medical Center Goettingen and the Animal Welfare Office of the state of Lower Saxony.

RT-PCR. Six organs of Corti were dissected and mRNA-isolated using TRIzol reagent (Invitrogen) according to the manufacturer's protocol. For RT, the GeneAmp RNA PCR Kit (Invitrogen) was applied and purified cDNA of *Cabp2*$^{+/+}$ and *Cabp2*$^{LacZ/LacZ}$ was amplified by the following primer combinations: PCR-1: forward (fwd) Exon1, reverse (rev) Exon5; PCR-2: fwdLacZ, revExon5; and PCR-3: fwdGAPDH, revGAPDH (primer list is provided in Table S1).

LacZ Staining. Cochleae and retinae were isolated and fixed for 10 min in 0.2% glutaraldehyde with 5 mM EGTA and 2 mM $MgCl_2$ in 100 mM PB. Tissue was washed three times for 15 min each time in detergent rinse solution containing 0.02% Igepal, 0.01% 7-deoxycholic acid sodium salt, and 2 mM $MgCl_2$ in 100 mM PBS (pH 7.3). For the staining reaction, samples were kept in X-Gal staining solution: 0.02% Igepal, 0.01% 7-deoxycholic acid, 5 mM $K_3Fe(CN)_6$, 5 mM $K_4Fe(CN)_6$, 2 mM $MgCl_2$, and 1 mg/mL X-Gal in 100 mM PBS (pH 7.3) overnight at 37 °C.

Transient Transfection of HEK 293/hSK3-1 Cells. HEK293/hSK3-1 cells were maintained in Dulbecco's modified Eagle medium/F12 Glutamax (GIBCO), containing 10% (vol/vol) FBS and 400 μg/mL G418 at 37 °C in a humidified atmosphere with 5% (vol/vol) CO_2 saturation. The cells were transfected with $Ca_V1.3\alpha1$ (AF370010, amount: 1×), β_{2A} (BC117468, amount: 0.5×), $\alpha_2\delta1$ (NM053851, amount: 0.5×), and CABP2-pEGFP-N1 (AB593136, amount: 0.05x) in ratios according to their length using the transfection reagent ExGen500 (Biomol) according to the manufacturer's protocol. The cells were used for electrophysiological recordings 36–48 h after transfection.

Patch-Clamp Recordings. An EPC-10 amplifier and PatchMaster software (HEKA) were used for whole-cell patch-clamp recordings utilizing low-pass filtering at 5 kHz, sampling at 50 kHz, and R_{series} compensation of 70% (R_{series} compensation for HEK293 cell experiments only). The external solution for HEK293 cell recordings contained the following: 150 mM choline Cl, 1 mM $MgCl_2$, 10 mM Cs-Hepes, 10 mM $CaCl_2$, and 100 nM apamin (pH 7.4 with methanesulfonic acid and osmolarity of 300–310 mOsm). The internal solution for HEK293 cell recordings contained the following: 140 mM *N*-methyl-D-glucamine, 5 mM EGTA, 10 mM NaCl, 1 mM $MgCl_2$, 10 mM Hepes, and 2 mM MgATP (pH 7.4, 290 mOsm). Recordings from IHCs were performed in the perforated- and ruptured-patch configurations. For the perforated-patch configuration, the pipette solution contained the following: 137 mM Cs-gluconate, 10 mM tetraethylammonium chloride (TEA-Cl), 10 mM 4-AP, 10 mM Cs-Hepes, 1 mM $MgCl_2$, and 300 μg/mL amphotericin B (pH 7.2, 283 mOsm). For the ruptured-patch configuration, the pipette solution contained the following: 134 mM Cs-gluconate, 10 mM TEA-Cl, 10 mM 4-AP, 10 mM Cs-Hepes, 1 mM $MgCl_2$, 0.5 mM EGTA, 0.5 mM BAPTA, 0.3 mM NaGTP, and 2 mM MgATP (pH 7.2, 283 mOsm). The standard bath solution contained the following: 113 mM NaCl, 35 mM TEA-Cl, 2.8 mM KCl, 1 mM CsCl, 1 mM $MgCl_2$, mM 10 NaOH-Hepes, 11.3 mM D-glucose, and $CaCl_2$ concentrations (pH 7.2, 300–310 mOsm). All patch-clamp experiments were performed at room temperature, except for the recordings in near-physiological conditions, which also used 1.3 mM $[Ca^{2+}]_e$. Cells were stimulated by depolarizations of different durations to −14 mV at intervals of 30–90 s. We measured and analyzed C_m as previously described (25). Exocytic C_m increments were analyzed as the difference between C_m during 400 ms before and after depolarization, skipping the first 100 ms after the end of the depolarizing pulse. All currents were leak-corrected subtracting the average and scaled passive current response, which was estimated from the responses to 10 subsequent depolarizations to 10% of the test depolarization and was multiplied by 10 (P/10). Voltage was corrected for liquid junction potentials calculated by the Patchers-Power-Tool of Igor-Pro (14 mV for perforated-patch experiments and 12.2 mV for HEK293/hSK3 recordings).

Systems Physiology: ABRs, Otoacoustic Emissions, and Electroretinography. For recordings of ABRs and DPOAEs, mice were anesthetized with a combination of i.p.-administered ketamine (125 mg/kg) and xylazine (2.5 mg/kg). The core temperature was maintained constant at 37 °C using a heat blanket (Hugo Sachs Elektronik–Harvard Apparatus). For stimulus generation, presentation, and data acquisition, we used the TDT II System run by BioSig software (Tucker Davis Technologies, MathWorks). Tone bursts (4/6/8/12/16/24/32 kHz, 10-ms plateau, 1-ms cos2 rise/fall) or clicks of 0.03 ms were presented at 40 Hz (tone bursts) or 20 Hz (clicks) in the free field ipsilaterally using a JBL

2402 speaker. The difference potential between vertex and mastoid subdermal needles was amplified 50,000-fold, filtered (400–4,000 Hz), and sampled at a rate of 50 kHz for 20 ms for a total of 1,300 times to obtain two mean ABR traces for each sound intensity. Hearing threshold was determined with 10-dB precision as the lowest stimulus intensity that evoked a reproducible response waveform in both traces by visual inspection by two independent observers.

For DPOAE, continuous primary tones (frequency f2 = 1.2 * f1, intensity l2 = l1–10 dB SPL) were delivered through a MF1 speaker system (Tucker Davis Technologies) and a custom-made probe containing an MKE-2 microphone (Sennheiser). The microphone signal was amplified (DMX 6Fire; Terratec), and the DPOAE amplitude at 2 * f2-f1 was analyzed by fast Fourier transformation using custom-written MATLAB software (MathWorks). SPLs are provided in SPL root mean square decibels (tonal stimuli) or SPL peak equivalent decibels (clicks). ERGs were recorded as in the study by tom Dieck et al. (63).

Single Auditory Nerve Fiber Recordings. Single-unit recordings were performed as described previously (43, 64, 65). In short, mice were anesthetized by i.p. injection of urethane (1.32 mg/kg), xylazine (5 mg/kg), and buprenorphine (0.1 mg/kg); tracheostomized; and placed in a stereotactic apparatus. After partial removal of the occipital bone and cerebellum, the internal auditory meatus was approached with a glass microelectrode passing through the posterior portion of the cochlear nucleus. Auditory nerve fibers were distinguished from cochlear nucleus neurons based on their stereotactic position (>1.2 mm from the surface of the cochlear nucleus, electrode aiming at the internal auditory canal) and response characteristics (poststimulus time histogram, regularity of firing, first-spike latency).

Immunohistochemistry. The apical coil of the organ of Corti was isolated from P21–P28 or P49–P61 mice and fixed with 4% (vol/vol) paraformaldehyde in PBS (15 min for synapse stains and 1 h for BK and SK2 staining). For Ca^{2+}-channel staining, the tissue was fixed in methanol for 20 min at −20 °C. After incubation of whole-mount preparations for 1 h in goat serum dilution buffer [16% (vol/vol) normal goat serum, 450 mM NaCl, 0.6% Triton X-100, 20 mM phosphate buffer (pH 7.4)], primary antibodies were applied overnight at 4 °C. The following antibodies were used: guinea pig anti–parvalbumin-α (1:200; Synaptic Systems), rabbit anti-BK (1:100; Alomone), mouse anti–α-calbindin D-28k (1:400; SWANT), rabbit anti-SK2 (1:200; Alomone), mouse IgG1 anti-CtBP2 (1:200; BD Biosciences, rabbit anti-GluA2/3 (1:200; Chemicon), and rabbit–anti-$Ca_V1.3$ (1:100; Alomone). Secondary AlexaFluor-labeled antibodies (1:200; Molecular Probes) were applied for 1 h at room temperature. Confocal images were collected using an SP5 microscope (Leica Microsystems) and analyzed with ImageJ software (NIH).

For immunostaining of retinal slices, retinae were fixed for 120 min in 4% (vol/vol) paraformaldehyde in PBS at room temperature, and were subsequently washed in PBS and transferred into sucrose gradient solutions of 10% (wt/vol; 10 min, room temperature), 20% (wt/vol; 2 h, room temperature), and 25% (wt/vol; overnight, 4 °C). After embedding the retina in cryomatrix (20 min; Life Technology), the tissue was frozen in a cryostat (−25 °C, 2800 Frigocut; Reichert–Jung), sliced (thickness of 60 μm), and stored at −80 °C until staining. The immunostaining procedure was the same as for the organs of Corti, just with chicken anti–β-galactosidase (1:100; Abcam) and mouse anti–α-calbindin D-28k (1:400). For anti–β-galactosidase antibody, a goat anti-chicken secondary AlexaFluor-labeled antibody (1:200; MoBiTec) was applied.

Protein Purification and Isothermal Titration Calorimetry. His6-tagged CABP2-wt (wild type) and GST-tagged CABP2-ΔEF3/4 were transformed into *Escherichia coli* BL21 (DE3) cells (Merck) and grown at 37 °C. The expression was induced with 0.5 M isopropyl 1-thio-β-D-galactopyranoside at A_{600} = 0.6 nm, and the temperature was set to 16 °C. After 15–20 h, the cells were harvested by centrifugation, resuspended in lysis buffer [20 mM Tris (pH 7.5), 300 mM NaCl, 10% (wt/wt) glycerol], and disrupted using a fluidizer (Mircofluidics). After centrifugation (45 min, 39086.1 × *g*), the obtained supernatant of the His6-tagged CABP2-wt protein was loaded onto a nickel-nitrilotriacetic acid column (GE Healthcare). To elute the protein, an elution gradient with imidazole-containing buffer [20 mM Tris (pH 7.5), 300 mM NaCl, 10% (vol/vol) glycerol, 500 mM imidazole] was performed, followed by size exclusion chromatography (S200 16/60; GE Healthcare) [20 mM Tris (pH 7.5), 300 mM NaCl, 10% (vol/vol) glycerol]. The GST-tagged CABP2-ΔEF3/4 protein was purified using a GST column (GE Healthcare) [20 mM Tris (pH 7.5), 300 mM NaCl, 10% (vol/vol) glycerol, elution buffer with 20 mM reduced glutathione], followed by size exclusion chromatography (S200 16/60) [20 mM Tris (pH 7.5), 300 mM NaCl, 10% (wt/wt) glycerol]. Both proteins were incubated with Chelex (Biorad) to remove remaining Ca^{2+} ions. During the purification steps, the temperature was kept at 4 °C.

Isothermal titration calorimetry was performed using a VP-ITC microcalorimeter (MicroCal/GE Healthcare). The reference cell was filled with buffer, and the protein was placed in the sample cell in the same buffer. Each experiment was performed at 8 °C with a protein concentration of 110 μM. The 5 mM $CaCl_2$ solution was prepared in buffer that was also treated with Chelex. Forty injections of 5 μL were added to the wild-type protein, and 35 injections of 5 μL were added to the mutant. To obtain a baseline after one injection, a time interval of 210 s was set; the used stirring speed was 307 rpm. Additionally, a titration of $CaCl_2$ in buffer was subtracted from the data to correct for heat of dilution. Each experiment was repeated three times. For data analysis and determination of the K_d, ΔH and ΔS values were measured using MicroCal Origin software running MicroCal/GE Healthcare ITC analysis routines.

Data Analysis. Voltage of half-maximal Ca^{2+} current ($V_{0.5}$) and activation constant (k_{act}) were calculated by first transforming the current–voltage (I-V) traces into an activation function: $I_{Ca} = g_{max}(V - V_{rev})$, where V describes the holding potential, V_{rev} the reversal potential, and g_{max} the maximum conductance. The activation function was fitted by a Boltzmann function: $1/(1 + \exp((V_{0.5}-V)/k_{act}))$. Data were analyzed using Igor Pro Software (Wavemetrics), Origin (MicroCal), and ImageJ. Means were expressed ± SEM and compared using two-tailed Student's *t* tests for normally distributed data of equal variance or else by the Wilcoxon rank sum test (if not stated otherwise), with $*P < 0.05$, $**P < 0.01$, and $***P < 0.005$, respectively.

ACKNOWLEDGMENTS. We thank Luis Pardo for supplying the HEK293/hSK3-1 cell line, and the KOMP repository (https://www.komp.org/) and the Welcome Trust Sanger Institute for providing us with the ES cell clone (DEPD0003_7_F06) to generate the *Cabp2*$^{LacZ/LacZ}$ strain used in this research project. We thank Tuck-Wah Soong, who provided us with the $Ca_V1.3$ plasmids. We thank S. Thom, S. Gerke, C. Senger-Freitag, G. Hoch, and C. Schmidt for expert technical assistance. We also thank C. Vogl for constant support and scientific discussion. This research was supported by grants from the German Research Foundation through the priority program 1608 (to T.M. and N.S.) and the Leibniz program (to T.M.), the Bernstein Center for Computational Neuroscience (Grant 01GQ1005A to T.M.), and the Flemish National Fund for Scientific Research (Grant KAN 1505013N to G.V.C.). In addition, this research was supported, in part, by a grant from Regione Lombardia, Italy (Innovative Research Project 1137-2010).

1. Safieddine S, El-Amraoui A, Petit C (2012) The auditory hair cell ribbon synapse: From assembly to function. *Annu Rev Neurosci* 35:509–528.
2. Wichmann C, Moser T (2015) Relating structure and function of inner hair cell ribbon synapses. *Cell Tissue Res* 361(1):95–114.
3. Brandt A, Striessnig J, Moser T (2003) CaV1.3 channels are essential for development and presynaptic activity of cochlear inner hair cells. *J Neurosci* 23(34):10832–10840.
4. Dou H, et al. (2004) Null mutation of alpha1D Ca2+ channel gene results in deafness but no vestibular defect in mice. *J Assoc Res Otolaryngol* 5(2):215–226.
5. Platzer J, et al. (2000) Congenital deafness and sinoatrial node dysfunction in mice lacking class D L-type Ca2+ channels. *Cell* 102(1):89–97.
6. Neef J, et al. (2009) The Ca2+ channel subunit beta2 regulates Ca2+ channel abundance and function in inner hair cells and is required for hearing. *J Neurosci* 29(34):10730–10740.
7. Fell B, et al. (2016) α2δ2 controls the function and trans-synaptic coupling of Cav1.3 channels in mouse inner hair cells and is essential for normal hearing. *J Neurosci* 36(43):11024–11036.
8. Brandt A, Khimich D, Moser T (2005) Few CaV1.3 channels regulate the exocytosis of a synaptic vesicle at the hair cell ribbon synapse. *J Neurosci* 25(50):11577–11585.
9. Johnson SL, Marcotti W, Kros CJ (2005) Increase in efficiency and reduction in Ca2+ dependence of exocytosis during development of mouse inner hair cells. *J Physiol* 563(Pt 1):177–191.
10. Koschak A, et al. (2001) alpha 1D (Cav1.3) subunits can form l-type Ca2+ channels activating at negative voltages. *J Biol Chem* 276(25):22100–22106.
11. Johnson SL, et al. (2011) Position-dependent patterning of spontaneous action potentials in immature cochlear inner hair cells. *Nat Neurosci* 14(6):711–717.
12. Russell IJ, Sellick PM (1983) Low-frequency characteristics of intracellularly recorded receptor potentials in guinea-pig cochlear hair cells. *J Physiol* 338:179–206.
13. Robertson D, Paki B (2002) Role of L-type Ca2+ channels in transmitter release from mammalian inner hair cells. II. Single-neuron activity. *J Neurophysiol* 87(6):2734–2740.
14. Lee A, et al. (1999) Ca2+/calmodulin binds to and modulates P/Q-type calcium channels. *Nature* 399(6732):155–159.
15. Peterson BZ, DeMaria CD, Adelman JP, Yue DT (1999) Calmodulin is the Ca2+ sensor for Ca2+-dependent inactivation of L-type calcium channels. *Neuron* 22(3):549–558.
16. Grant L, Fuchs P (2008) Calcium- and calmodulin-dependent inactivation of calcium channels in inner hair cells of the rat cochlea. *J Neurophysiol* 99(5):2183–2193.

17. Weiler S, Krinner S, Wong AB, Moser T, Pangršič T (2014) ATP hydrolysis is critically required for function of CaV1.3 channels in cochlear inner hair cells via fueling Ca2+ clearance. *J Neurosci* 34(20):6843–6848.
18. Cui G, et al. (2007) Ca2+-binding proteins tune Ca2+-feedback to Cav1.3 channels in mouse auditory hair cells. *J Physiol* 585(Pt 3):791–803.
19. Yang PS, et al. (2006) Switching of Ca2+-dependent inactivation of Ca(v)1.3 channels by calcium binding proteins of auditory hair cells. *J Neurosci* 26(42):10677–10689.
20. Bock G, et al. (2011) Functional properties of a newly identified C-terminal splice variant of Cav1.3 L-type Ca2+ channels. *J Biol Chem* 286(49):42736–42748.
21. Singh A, et al. (2008) Modulation of voltage- and Ca2+-dependent gating of CaV1.3 L-type calcium channels by alternative splicing of a C-terminal regulatory domain. *J Biol Chem* 283(30):20733–20744.
22. Tan BZ, et al. (2011) Functional characterization of alternative splicing in the C terminus of L-type CaV1.3 channels. *J Biol Chem* 286(49):42725–42735.
23. Goutman JD, Glowatzki E (2007) Time course and calcium dependence of transmitter release at a single ribbon synapse. *Proc Natl Acad Sci USA* 104(41):16341–16346.
24. Li GL, Keen E, Andor-Ardó D, Hudspeth AJ, von Gersdorff H (2009) The unitary event underlying multiquantal EPSCs at a hair cell's ribbon synapse. *J Neurosci* 29(23): 7558–7568.
25. Moser T, Beutner D (2000) Kinetics of exocytosis and endocytosis at the cochlear inner hair cell afferent synapse of the mouse. *Proc Natl Acad Sci USA* 97(2):883–888.
26. Furukawa T, Matsuura S (1978) Adaptive rundown of excitatory post-synaptic potentials at synapses between hair cells and eight nerve fibres in the goldfish. *J Physiol* 276:193–209.
27. Haeseleer F, et al. (2000) Five members of a novel Ca(2+)-binding protein (CABP) subfamily with similarity to calmodulin. *J Biol Chem* 275(2):1247–1260.
28. Haeseleer F, Imanishi Y, Sokal I, Filipek S, Palczewski K (2002) Calcium-binding proteins: Intracellular sensors from the calmodulin superfamily. *Biochem Biophys Res Commun* 290(2):615–623.
29. Kinoshita-Kawada M, et al. (2005) Inhibition of TRPC5 channels by Ca2+-binding protein 1 in Xenopus oocytes. *Pflugers Arch* 450(5):345–354.
30. Yang J, et al. (2002) Identification of a family of calcium sensors as protein ligands of inositol trisphosphate receptor Ca(2+) release channels. *Proc Natl Acad Sci USA* 99(11):7711–7716.
31. Hackney CM, Mahendrasingam S, Penn A, Fettiplace R (2005) The concentrations of calcium buffering proteins in mammalian cochlear hair cells. *J Neurosci* 25(34):7867–7875.
32. Pack AK, Slepecky NB (1995) Cytoskeletal and calcium-binding proteins in the mammalian organ of Corti: Cell type-specific proteins displaying longitudinal and radial gradients. *Hear Res* 91(1-2):119–135.
33. Schwaller B, Meyer M, Schiffmann S (2002) 'New' functions for 'old' proteins: The role of the calcium-binding proteins calbindin D-28k, calretinin and parvalbumin, in cerebellar physiology. Studies with knockout mice. *Cerebellum* 1(4):241–258.
34. Yang T, et al. (2016) Expression and localization of CaBP Ca2+ binding proteins in the mouse cochlea. *PLoS One* 11(1):e0147495.
35. Schrauwen I, et al. (2012) A mutation in CABP2, expressed in cochlear hair cells, causes autosomal-recessive hearing impairment. *Am J Hum Genet* 91(4):636–645.
36. Haeseleer F, et al. (2004) Essential role of Ca2+-binding protein 4, a Cav1.4 channel regulator, in photoreceptor synaptic function. *Nat Neurosci* 7(10):1079–1087.
37. Kujawa SG, Liberman MC (2009) Adding insult to injury: cochlear nerve degeneration after "temporary" noise-induced hearing loss. *J Neurosci* 29(45):14077–14085.
38. Meyer NC, et al. (2007) Identification of three novel TECTA mutations in Iranian families with autosomal recessive nonsyndromic hearing impairment at the DFNB21 locus. *Am J Med Genet A* 143A(14):1623–1629.
39. Lakso M, et al. (1996) Efficient in vivo manipulation of mouse genomic sequences at the zygote stage. *Proc Natl Acad Sci USA* 93(12):5860–5865.
40. Moser T, Starr A (2016) Auditory neuropathy–neural and synaptic mechanisms. *Nat Rev Neurol* 12(3):135–149.
41. Khimich D, et al. (2005) Hair cell synaptic ribbons are essential for synchronous auditory signalling. *Nature* 434(7035):889–894.
42. Pangršič T, et al. (2015) EF-hand protein Ca2+ buffers regulate Ca2+ influx and exocytosis in sensory hair cells. *Proc Natl Acad Sci USA* 112(9):E1028–E1037.
43. Taberner AM, Liberman MC (2005) Response properties of single auditory nerve fibers in the mouse. *J Neurophysiol* 93(1):557–569.
44. Tabatabaiefar MA, et al. (2011) DFNB93, a novel locus for autosomal recessive moderate-to-severe hearing impairment. *Clin Genet* 79(6):594–598.
45. Ohn T-L, et al. (2016) Hair cells use active zones with different voltage dependence of Ca2+ influx to decompose sounds into complementary neural codes. *Proc Natl Acad Sci USA* 113(32):E4716–E4725.
46. Scharinger A, et al. (2015) Cell-type-specific tuning of Cav1.3 Ca(2+)-channels by a C-terminal automodulatory domain. *Front Cell Neurosci* 9:309.
47. Kuhn S, et al. (2009) Ba2+ currents in inner and outer hair cells of mice lacking the voltage-dependent Ca2+ channel subunits beta3 or beta4. *Channels (Austin)* 3(5): 366–376.
48. Gebhart M, et al. (2010) Modulation of Cav1.3 Ca2+ channel gating by Rab3 interacting molecule. *Mol Cell Neurosci* 44(3):246–259.
49. Jung S, et al. (2015) Rab3-interacting molecules 2α and 2β promote the abundance of voltage-gated CaV1.3 Ca2+ channels at hair cell active zones. *Proc Natl Acad Sci USA* 112(24):E3141–E3149.
50. Gregory FD, et al. (2011) Harmonin inhibits presynaptic Cav1.3 Ca^{2+} channels in mouse inner hair cells. *Nat Neurosci* 14(9):1109–1111.
51. Gregory FD, Pangrsic T, Calin-Jageman IE, Moser T, Lee A (2013) Harmonin enhances voltage-dependent facilitation of Cav1.3 channels and synchronous exocytosis in mouse inner hair cells. *J Physiol* 591(13):3253–3269.
52. Lee A, et al. (2002) Differential modulation of Ca(v)2.1 channels by calmodulin and Ca2+-binding protein 1. *Nat Neurosci* 5(3):210–217.
53. Shen Y, et al. (2006) Alternative splicing of the Ca(v)1.3 channel IQ domain, a molecular switch for Ca2+-dependent inactivation within auditory hair cells. *J Neurosci* 26(42):10690–10699.
54. Tong B, et al. (2016) Oncomodulin, an EF-hand Ca2+ buffer, is critical for maintaining cochlear function in mice. *J Neurosci* 36(5):1631–1635.
55. Findeisen F, Minor DL, Jr (2010) Structural basis for the differential effects of CaBP1 and calmodulin on Ca(V)1.2 calcium-dependent inactivation. *Structure* 18(12): 1617–1631.
56. Findeisen F, Rumpf CH, Minor DL, Jr (2013) Apo states of calmodulin and CaBP1 control CaV1 voltage-gated calcium channel function through direct competition for the IQ domain. *J Mol Biol* 425(17):3217–3234.
57. Dafi O, et al. (2004) Negatively charged residues in the N-terminal of the AID helix confer slow voltage dependent inactivation gating to CaV1.2. *Biophys J* 87(5): 3181–3192.
58. Tadross MR, Yue DT (2010) Systematic mapping of the state dependence of voltage- and Ca2+-dependent inactivation using simple open-channel measurements. *J Gen Physiol* 135(3):217–227.
59. Fei J, Shiming Y (2012) Diagnosis and treatment of auditory neuropathy and related research. *J Otol* 7:86–91.
60. Rodríguez-Ballesteros M, et al. (2003) Auditory neuropathy in patients carrying mutations in the otoferlin gene (OTOF). *Hum Mutat* 22(6):451–456.
61. Li G-L, Cho S, von Gersdorff H (2014) Phase-locking precision is enhanced by multiquantal release at an auditory hair cell ribbon synapse. *Neuron* 83(6):1404–1417.
62. Skarnes WC, et al. (2011) A conditional knockout resource for the genome-wide study of mouse gene function. *Nature* 474(7351):337–342.
63. tom Dieck S, et al. (2012) Deletion of the presynaptic scaffold CAST reduces active zone size in rod photoreceptors and impairs visual processing. *J Neurosci* 32(35): 12192–12203.
64. Frank T, et al. (2010) Bassoon and the synaptic ribbon organize Ca^2+ channels and vesicles to add release sites and promote refilling. *Neuron* 68(4):724–738.
65. Jing Z, et al. (2013) Disruption of the presynaptic cytomatrix protein bassoon degrades ribbon anchorage, multiquantal release, and sound encoding at the hair cell afferent synapse. *J Neurosci* 33(10):4456–4467.